Chem

CellPress

Article

Design Principles for High-Capacity Mn-Based Cation-Disordered Rocksalt Cathodes

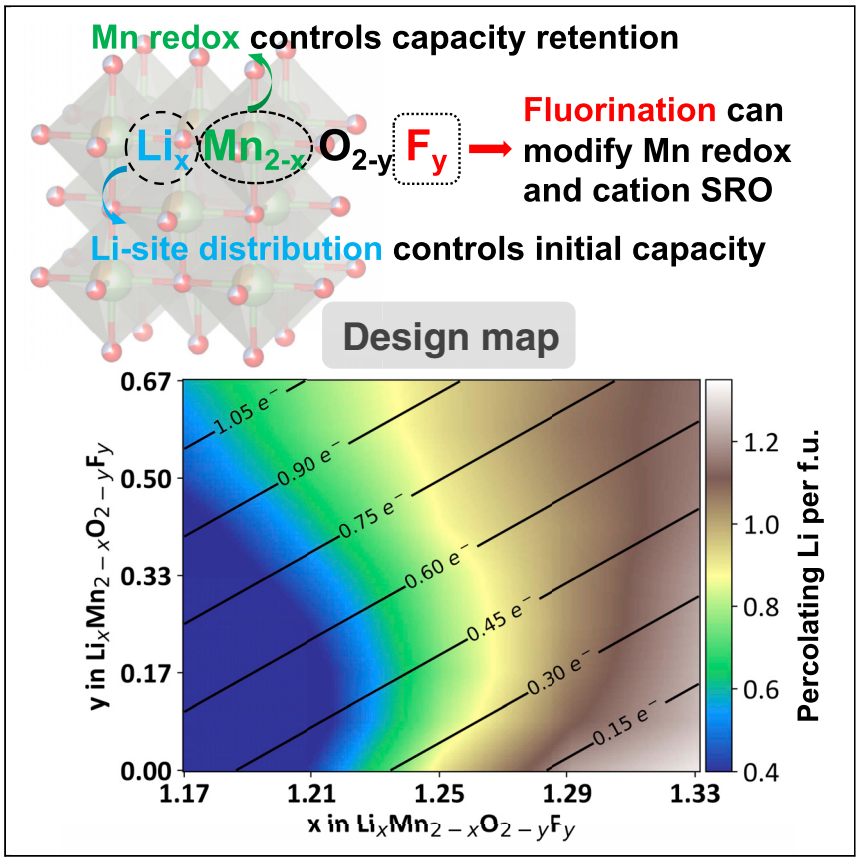

The discovery of Li-excess cation-disordered rocksalt (DRX) cathodes greatly enlarges the design space beyond the layered NCM-type rocksalt chemistries. More importantly, this new strategy enables high-capacity Co- and Ni-free cathodes, a requirement for the Li-ion industry to grow to the Terra-Wh scale, which is needed for growing electric-vehicle and utility applications. Here, we rationalize the compositional design principles in Li-Mn-O-F DRX space, which is particularly promising due to its high-energy density, low-cost chemistry, and compositional flexibility.

Zhengyan Lun, Bin Ouyang, Zijian Cai, ..., Haegyeom Kim, Daniil A. Kitchaev, Gerbrand Ceder

gceder@berkeley.edu

HIGHLIGHTS

Li-rich Mn-based cation-disordered rocksalts enable high-energy Li-ion cathodes

Li-site distribution controls the initial capacity of the Li-Mn-O-F DRX cathodes

Mn-redox capacity strongly influences the cyclability of Li-Mn-O-F DRX cathodes

Lun et al., Chem 6, 153–168
January 9, 2020 © 2019 Elsevier Inc.
https://doi.org/10.1016/j.chempr.2019.10.001

Chem

CellPress

Article

Design Principles for High-Capacity Mn-Based Cation-Disordered Rocksalt Cathodes

Zhengyan Lun,[1,2,7] Bin Ouyang,[1,2,7] Zijian Cai,[1,2] Raphaële J. Clément,[1,8] Deok-Hwang Kwon,[1,2] Jianping Huang,[2] Joseph K. Papp,[4] Mahalingam Balasubramanian,[3] Yaosen Tian,[1,2] Bryan D. McCloskey,[4,5] Huiwen Ji,[1,2,5] Haegyeom Kim,[2] Daniil A. Kitchaev,[6,8] and Gerbrand Ceder[1,2,9,*]

SUMMARY

Mn-based Li-excess cation-disordered rocksalt (DRX) oxyfluorides are promising candidates for next-generation rechargeable battery cathodes owing to their large energy densities, the earth abundance, and low cost of Mn. In this work, we synthesized and electrochemically tested four representative compositions in the Li-Mn-O-F DRX chemical space with various Li and F content. While all compositions achieve higher than 200 mAh g^{-1} initial capacity and good cyclability, we show that the Li-site distribution plays a more important role than the metal-redox capacity in determining the initial capacity, whereas the metal-redox capacity is more closely related to the cyclability of the materials. We apply these insights and generate a capacity map of the Li-Mn-O-F chemical space, $Li_xMn_{2-x}O_{2-y}F_y$ ($1.167 \leq x \leq 1.333$, $0 \leq y \leq 0.667$), which predicts both accessible Li capacity and Mn-redox capacity. This map allows the design of compounds that balance high capacity with good cyclability.

INTRODUCTION

The tremendous success and growth of Li-ion-based energy storage in a broad range of applications[1,2] are likely to strain our natural resources.[3] Projected growth of Li-ion production toward 1 TWh/year will require more than a million tons of Co and Ni combined, which constitutes a very sizable fraction of the annual production of these metals.[4] The recent development of Li-excess cation-disordered rocksalt (DRX) cathodes[5–7] is providing an avenue for the Li-ion battery field to develop high-energy-density cathodes with more abundant and less expensive metals. In these DRX compounds, Li migrates through a percolating network of so-called "0-TM" clusters in which the absence of transition metals (TMs) at the activated state enables facile migration.[5,6] Lifting the restriction that cathode structures must be layered and remain layered during electrochemical cycling has enabled the exploration of a much wider chemical space beyond the traditional Ni-Co-Mn (NCM) space.[5,8–17] In addition, the ability to substitute some of the oxygen by fluorine in locally Li-rich environments in DRX structures provides an extra handle to optimize performance by introducing additional metal-redox capacity[8,15,18] and improve cyclability.[13,18]

Mn is a particularly promising redox-active element for cathodes because of its low cost and natural abundance. In addition, fully charged Mn-cathodes contain Mn^{4+}, which is a stable valence state, thereby enhancing the thermal stability of cathode

The Bigger Picture

Moving Li-ion to Terra-Wh scale annual production will require a move away from the current Co- and Ni-based cathode materials. Recently developed cation-disordered rocksalt (DRX) cathodes greatly expanded the current chemical space with which to create high-energy-density cathodes to more abundant and inexpensive metals, such as Mn. Here, we demonstrate four well-selected compositions in the Li-Mn-O-F DRX chemical space and investigate their electrochemical performances, redox behaviors, and Li-site distributions. We find that while all their capacities are high, initial capacity and cycle life can be traded off to some extent. Initial capacity is mainly controlled by the Li percolation network, while the amount of metal redox strongly influences the cyclability. Several trade-offs between Li-excess level, F content, and metal-redox content are discussed and presented in the form of a design map, serving as guidance for future experimental explorations in the Li-Mn-O-F chemical space.

materials. The Mn^{3+}/Mn^{4+} redox couple is active in $LiMn_2O_4$ spinel cathodes but can only be partially utilized because of the collective Jahn-Teller distortion upon full reduction to Mn^{3+}.[19] Recently, the highly F-substituted DRX compounds $Li_2Mn_{2/3}Nb_{1/3}O_2F$ and $Li_2Mn_{1/2}Ti_{1/2}O_2F$ were shown to have very high capacity with two-electron Mn^{2+} to Mn^{4+} oxidation.[8] Other high-capacity Mn-compounds include $Li_4Mn_2O_5$, which was argued to utilize a combination of Mn^{3+}/Mn^{4+}, O^{2-}/O^{-}, and Mn^{4+}/Mn^{5+} redox, but experiences severe capacity fading upon extended cycling.[10] In $Li_{1.9}Mn_{0.95}O_{2.05}F_{0.95}$, partial fluorine substitution was applied to improve cyclability.[15] In another example, V^{4+} was applied as a charge compensator in $Li_{1.171}Mn_{0.343}V_{0.486}O_{1.8}F_{0.2}$ to obtain additional electron capacity from the V^{4+}/V^{5+} redox in addition to that provided by the Mn^{2+}/Mn^{4+} redox.[14]

These initial results demonstrate that the Li-Mn-O-F chemical space may be particularly important for finding high-capacity, low-cost cathodes. Optimization of these materials is likely to involve several trade-offs. The Li excess required for good transport in disordered rocksalts reduces the TM-electron capacity, necessitating oxygen redox to achieve high capacity. Fluorine substitution on anion sites can negate this to some extent by lowering the average valence requirement on the cations. At the same time, F incorporation is expected to change the Li percolation network due to the large bonding preference between Li and F over Mn and F.[20] In this paper, we systematically investigate the role of each compositional handle (Li excess, TM redox capacity, and F content) on the initial discharge capacity and cycle life within the compositional space $Li_xMn_{2-x}O_{2-y}F_y$ ($1.167 \leq x \leq 1.333$, $0 \leq y \leq 0.667$). We use *ab initio* simulations to study how Li percolation is modified by short-range order (SRO), previously shown to significantly affect the Li environments, their percolation, and ultimately the Li transport of DRX materials[21–24] and correlate it to measured electrochemical performance and spectroscopic information.

We synthesize, characterize, model, and electrochemically test four well-chosen compositions within the Li–Mn–O–F DRX chemical space with different Li content and F content: $Li_{1.3333}Mn(III)_{0.6667}O_{1.3333}F_{0.6667}$, $Li_{1.3333}Mn(III)_{0.5}Mn(IV)_{0.1667}O_{1.5}F_{0.5}$, $Li_{1.3333}Mn(III)_{0.3333}Mn(IV)_{0.3333}O_{1.6667}F_{0.3333}$, and $Li_{1.25}Mn(II)_{0.1667}Mn(III)_{0.5833}O_{1.3333}F_{0.6667}$, hereafter referred to as HLF67, HLF50, HLF33, and LLF67, respectively, with "HL" referring to "high Li content" (1.3333 per formula unit [f.u.]), "LL" referring to "low Li content" (1.25 per f.u.), and numbers denoting the F content. For one group of samples, the Li content is kept the same and the F content is gradually decreased from HLF67, HLF50, and HLF33, so that progressively less TM redox capacity is expected because of the incorporation of more Mn^{4+} ions in the as-synthesized material to maintain charge balance. For the other group, HLF67 and LLF67 are used to contrast Li capacity versus TM capacity. These samples have the same F content, but Li excess is lowered in LLF67 in order to create more Mn^{2+} giving more TM redox capacity. The redox behavior of these compounds is investigated by combining spectroscopic methods and density functional theory (DFT) calculations, while SRO in the materials is studied using a combined DFT and Monte Carlo method, which is also experimentally confirmed by neutron-pair distribution function (NPDF) measurement. Our investigations reveal that the nature of the Li network and its percolation properties play a more important role than the metal-redox capacity in determining the initial capacity of the compounds, whereas the metal-redox capacity has a greater effect on the capacity retention. We then apply these insights and expand our computational analysis to a larger compositional space within the Li-Mn-O-F chemistry and construct a capacity map to provide more practical guidance for experimental design.

[1]Department of Materials Science and Engineering, UC Berkeley, Berkeley, CA 94720, USA

[2]Materials Sciences Division, LBNL, Berkeley, CA 94720, USA

[3]X-Ray Science Division, Advanced Photon Source, Argonne National Laboratory, Argonne, IL 60439, USA

[4]Department of Chemical and Biomolecular Engineering, UC Berkeley, Berkeley, CA 94720, USA

[5]Energy Storage and Distributed Resources Division, LBNL, Berkeley, CA 94720, USA

[6]Department of Materials Science and Engineering, MIT, Cambridge, MA 02139, USA

[7]These authors contributed equally

[8]Present address: Materials Department, University of California, Santa Barbara, Santa Barbara, CA 93106, USA

[9]Lead Contact

*Correspondence: gceder@berkeley.edu

https://doi.org/10.1016/j.chempr.2019.10.001

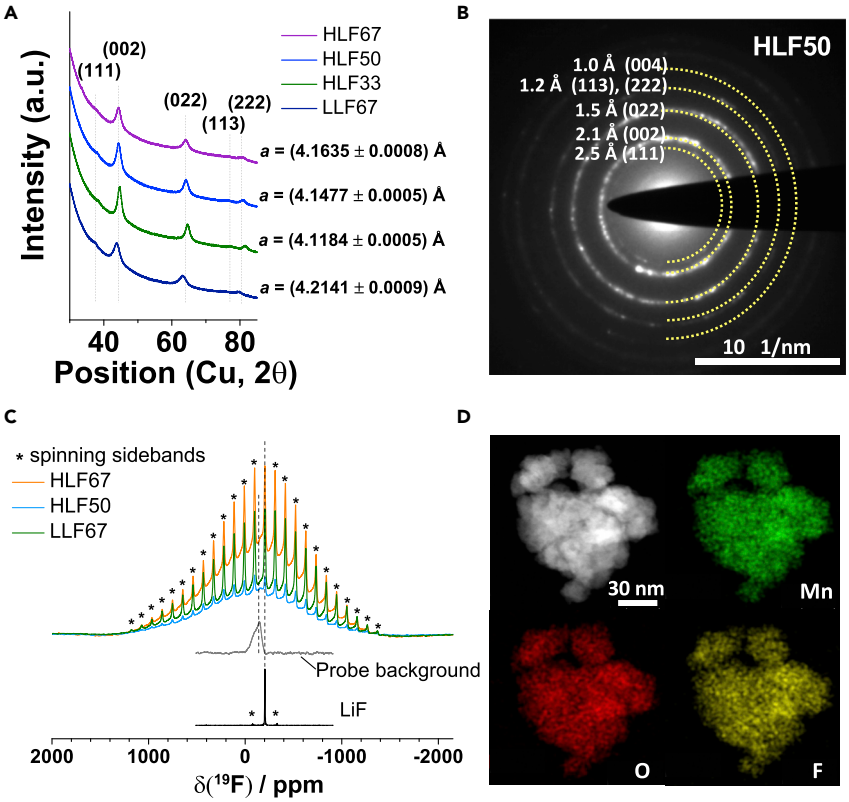

Figure 1. Structural Characterization of the As-Synthesized Li-Mn-O-F Compounds

(A) XRD patterns and refined lattice constants of the as-synthesized materials.

(B) Electron diffraction pattern of as-synthesized HLF50.

(C) ^{19}F frequency-stepping spectra obtained for the as-synthesized HLF67, HLF50, and LLF67 powders by summing over nine spin-echo sub-spectra acquired at different excitation frequencies. The spectra are scaled according to the amount of sample in the rotor. For comparison, ^{19}F spin-echo spectra collected on LiF powder and on an empty rotor (to measure the probe background signal) are overlaid. The shoulder observed to the left of the most intense peak in the spectra, at ca. −163 ppm, is ascribed to the probe background signal. Spinning sidebands of the sharp, diamagnetic signals are indicated with asterisks.

(D) TEM EDS mapping of the elemental distribution in a particle cluster of as-synthesized HLF50. Scale bar: 30 nm.

RESULTS

Structural Characterization

The four compounds were synthesized using a mechanochemical ball-milling method (see Experimental Procedures). The X-ray diffraction (XRD) patterns shown in Figure 1A confirm that all the materials form a DRX structure with no observable impurity peaks. In addition, elemental analysis confirmed that the compositions of the materials are close to the target compositions, as shown in Table S1. The difference in lattice constants of the materials is consistent with the degree of Mn oxidation. The presence of more Mn^{4+} reduces the lattice constant from 4.1635 ± 0.0008 Å (HLF67) to 4.1477 ± 0.0005 Å (HLF50) and 4.1184 ± 0.0005 Å (HLF33), whereas the introduction of large Mn^{2+} ions increases the lattice constant to 4.2141 ± 0.0009 Å for LLF67 despite the reduction in Li content. The F-to-O ratio appears less significant in determining the lattice constant, consistent with their small difference in ionic radius.[25] Detailed refinements of the XRD patterns are presented in Figure S1. Transmission electron microscopy (TEM) electron diffraction (ED) patterns of the as-synthesized materials also show phase-pure DRX without

observable impurities (Figures 1B and S4). Nanosized small grains with different orientations pack closely together to form a polycrystalline primary particle (Figure S4), the size of which is in the range of 100–200 nm for as-synthesized materials, as observed in the scanning electron microscopy (SEM) images in Figure S2.

Although no LiF impurity phases were detected using XRD and TEM ED techniques, we called on ^{19}F solid-state nuclear magnetic resonance spectroscopy (ssNMR) to further confirm that most of the fluorine is incorporated within the bulk material rather than forming a separate LiF phase. The ^{19}F NMR spectra collected on HLF67, HLF50, and LLF67 powders, as well as on LiF powder and an empty rotor for reference, are presented in Figure 1C. While the small shoulder at approximately −163 ppm originates from the probe background, we find that the ^{19}F NMR spectra collected on the various cathode materials differ significantly from that of the LiF reference. The former spectra are composed of a number of broad, overlapping signals shifted away from the resonance frequency of LiF at −204 ppm. As discussed in previous NMR studies on related oxyfluoride materials,[8,13,14,18,21] these broad features arise from strong paramagnetic interactions from short-range paramagnetic interactions between unpaired *d* electrons on Mn ions and the F nucleus, which confirms the bulk incorporation of F into the disordered rocksalt phase.[6] When F is directly bonded to Mn ions, paramagnetic interactions are so strong that the resulting signals are too broad to be detectable and are lost in the background noise. These invisible paramagnetic F sites prevent us from quantifying the fraction of F in LiF-like domains or particles in the pristine cathode samples, as evidenced by the sharp signal centered at ∼204 ppm and present in all spectra. Nevertheless, the present data indicate that the vast majority of the fluorine of the as-synthesized materials is incorporated into the particles. ^{7}Li NMR spectra are also presented in Figure S3. Note S1 discusses the problem of attributing the ∼0 ppm signal to either impurities or to the possible formation of diamagnetic Li-rich (Mn-poor) domains within the disordered oxide matrix. Finally, TEM energy dispersive spectroscopy (EDS) mapping images are shown in Figures 1D and S4 and indicate a homogeneous distribution of F throughout the particles, which further confirms the bulk substitution of F.

Electrochemical Performance

The electrochemical performance of the Li-Mn-O-F compounds was tested in galvanostatic mode at 20 mA g^{-1} and room temperature within different voltage windows (1.5–4.6, 4.8, and 5.0 V). Figure 2A summarizes the first cycle discharge capacities, average voltages, and specific energies for all of the compounds. Figure 2B presents the voltage profiles of HLF67, HLF50, HLF33, and LLF67 for the first cycle between 1.5 and 4.8 V; the compounds exhibit discharge capacities (specific energies) of 259 mAh g^{-1} (844 Wh kg^{-1}), 284 mAh g^{-1} (909 Wh kg^{-1}), 336 mAh g^{-1} (1059 Wh kg^{-1}), and 242 mAh g^{-1} (771 Wh kg^{-1}), respectively. When cycling between 1.5 and 5.0 V, their initial discharge capacities (specific energies) increase to 290 mAh g^{-1} (950 Wh kg^{-1}), 319 mAh g^{-1} (1,016 Wh kg^{-1}), 349 mAh g^{-1} (1,068 Wh kg^{-1}), and 256 mAh g^{-1} (822 Wh kg^{-1}), respectively, as shown in Figure 2C.

Figures 2D–2F present the representative voltage profiles for HLF67, HLF33, and LLF67 and their capacity retention, when cycling between 1.5 and 5.0 V. The red dashed lines indicate the theoretical Mn-redox capacities in each compound. HLF67 exhibits an initial capacity (specific energy) of 290 mAh g^{-1} (950 Wh kg^{-1}) and good capacity retention (Figure 2D). HLF33 shows a larger initial capacity (specific energy) of 349 mAh g^{-1} (1,068 Wh kg^{-1}) but somewhat worse capacity retention than that of HLF67 (Figure 2E). LLF67 shows a lower initial capacity (specific energy)

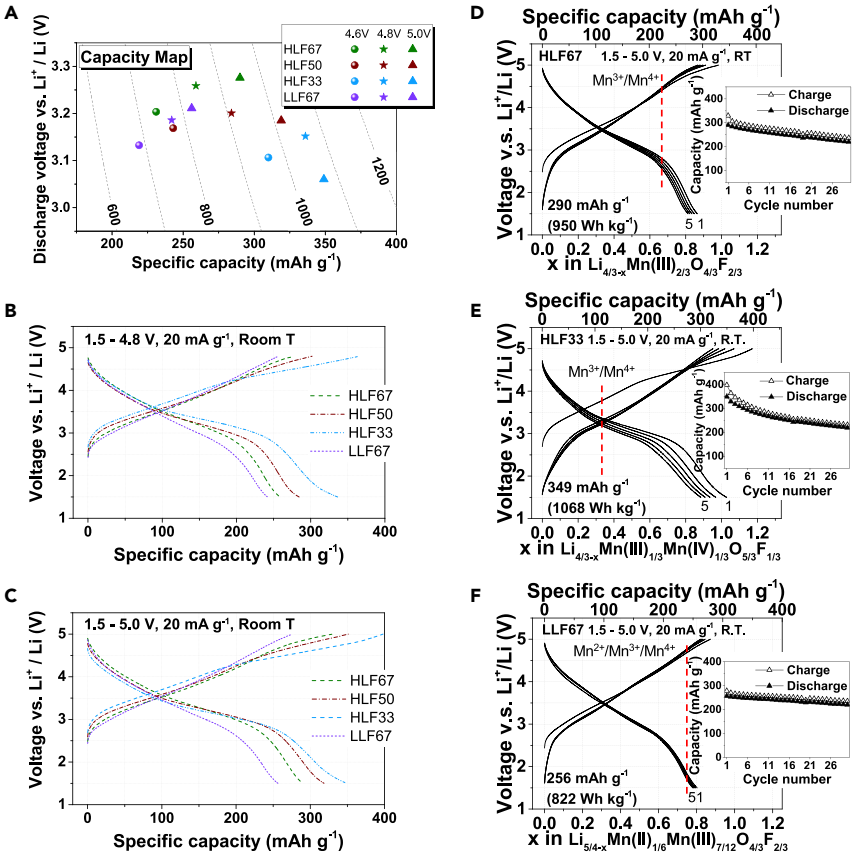

Figure 2. Electrochemical Performance of Li-Mn-O-F Compounds

(A) Capacity map showing initial discharge capacities and energy densities of Li-Mn-O-F compounds at different voltage windows.

(B and C) First cycle voltage profiles of Li-Mn-O-F compounds within the voltage windows of 0.5–4.8 V (B) and 1.5–5.0 V (C) at a rate of 20 mA g^{-1} at room temperature.

(D–F) Representative voltage profiles and capacity retention of HLF67 (D), HLF33 (E), and LLF67 (F) within the voltage window of 1.5–5.0 V at 20 mA g^{-1} at room temperature. The red dashed lines indicate the theoretical Mn-redox capacities. The initial oxidation states of Mn in the as-synthesized materials can be found from the bottom x axis.

of 256 mAh g^{-1} (822 Wh kg^{-1}) than HLF67 but shows improved cyclability, with less than 15% capacity fading over the first 30 cycles (Figure 2F). More electrochemical cycling results are presented in Figure S5.

In order to understand the relation between composition and electrochemical performance, the redox mechanism and local SRO in these compounds are carefully studied in the following sections.

Redox Mechanism

The redox mechanisms of the Li-Mn-O-F compounds were investigated using *ex situ* hard X-ray absorption spectroscopy (XAS) and *ab initio* calculations. The top panel of Figure 3A shows the Mn K-edge X-ray near-edge structure (XANES) of all four pristine compounds. The Mn K-edge energy increases in the order of LLF67 < HLF67 < HLF50 < HLF33. At the top of charge, the Mn^{3+}/Mn^{4+} redox process is almost complete in HLF50 and HLF33, while Mn ions in HLF67 and LLF67 are oxidized to a lesser extent, as shown in the lower panel of Figure 3A.

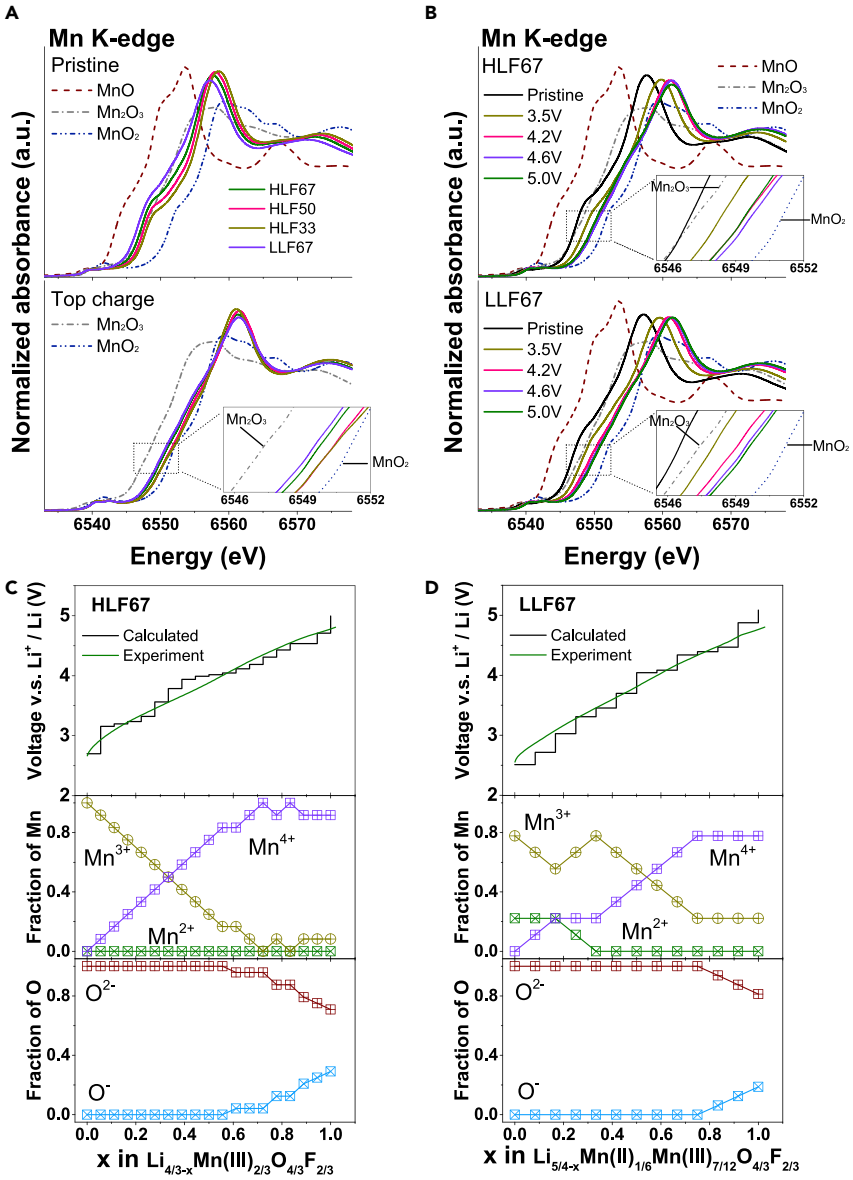

Figure 3. Redox Mechanism of Li-Mn-O-F Compounds

(A) Mn K-edge XANES spectra of all compounds at the pristine state and top charge in the first cycle.

(B) Mn K-edge XANES spectra of HLF67 and LLF67 at different states of charge in the initial cycle.

(C and D) Computed voltage profiles and evolution of Mn and O oxidation states calculated from DFT, denoting the dominant electron capacity source at each state of delithiation for HLF67 (C) and LLF67 (D). The experimental voltage profiles overlaid in the figures of each compound are the quasi-equilibrium voltage profiles obtained from potentiostatic intermittent titration technique (PITT) measurements when charged from open circuit voltage to 4.8 V.

This finding is consistent with the observation by Lee et al. that a large lattice constant and the presence of more Mn-F bonds create more overlap between Mn and O redox and can prevent Mn from being fully oxidized to Mn^{4+}.[8] These interpretations are further supported by the Mn pre-edge derivative analysis, as presented in Figure S6 and Note S2.

To compare the oxidation behavior of Mn in HLF67 and LLF67, we select five points at different states of charge in the first charge: the pristine state and charged to 3.5, 4.2, 4.6, and 5.0 V as shown in Figure 3B. In general, similar redox behavior is observed for the two compounds: Mn oxidation dominates at low voltage, but at high voltage, the Mn K-edge barely shifts, indicating limited Mn redox. However, a small shift of the edge position to a lower energy at high voltage is observed in HLF67 but not in LLF67; this shift has been ascribed to the partial reduction of the TM (Mn in this case) due to oxygen oxidation.[26] Partial reduction of Mn at high voltage is also observed in HLF50 and HLF33, as shown in Figures S7A and S7B, which suggests that the participation of oxygen redox processes in the overall charge compensation mechanism is more significant in HLF67, HLF50, and HLF33 than in LLF67.

To obtain further insight into the oxidation mechanisms in these cathode materials, we used DFT to calculate the voltage curves and the evolution of Mn and O oxidation states upon delithiation. Figures 3C and 3D show the calculated redox mechanisms for HLF67 and LLF67, respectively. It is clear that oxygen redox happens earlier in HLF67 than in LLF67 and contributes more to the overall capacity, consistent with the presence of more Li excess in HLF67 to facilitate oxygen oxidation.[27] As a result, Mn partial reduction is observed in HLF67 at the top of charge but not in LLF67. At the top of charge, Mn is less oxidized in LLF67 than in HLF67, which is consistent with the XAS observations.

Combining the electrochemical performance and the redox-center data establishes a clear correlation between the charge compensation process and the capacity retention of the compounds; with an increasing contribution of oxygen redox from LLF67 to HLF67, HLF50, and HLF33, the capacity retention of the materials gradually decreases. Oxygen redox is generally considered to lead to less stable cycling compared to metal redox since it triggers irreversible oxygen loss, leaving behind a metal-densified surface layer, which hinders Li transport. Fluorination is an effective way to lower the average cation oxidation states, enabling the incorporation of more metal redox to improve the capacity retention. Consistently, the amount of irreversible oxygen loss is reduced in the order of HLF33 > HLF50 > LLF67, as can be observed from the differential electrochemical mass spectroscopy (DEMS) results (shown in Figure S8).

Short-Range Order Analysis

The short-range order (SRO) in the Li-Mn-O-F compounds was investigated using a cluster expansion Hamiltonian parameterized by DFT total energy calculations. As the Li network significantly affects the electrochemical performance of DRX compounds,[23] we first evaluate the frequency of tetrahedra that are only occupied by Li ions (the 0-TM Li_4 tetrahedra) in the four compounds as this is the environment through which Li migrates. Figure 4A shows the fraction of tetrahedra that are 0-TM in the simulated Li-Mn-O-F compounds at 2,573 K as well as in the random limit (infinite temperature). As calibrated in previous work[20] the temperature of 2,573 K was chosen as a proxy for the high-energy conditions with which disorder is generated with ball milling in the Li-Mn-O-F chemical space but should not be taken as a particularly significant value. The structures generated at 2,573 K show good agreement with the materials obtained experimentally, as discussed in Figure S10 and Note S4. The "random limit" cation configuration in the structure is one where the cations are distributed completely randomly over the cation lattice, only satisfying the concentration requirement. Such a configuration has no SRO and can be used as a reference. Comparing the 0-TM occurrence in HLF67, HLF50, and HLF33, it is

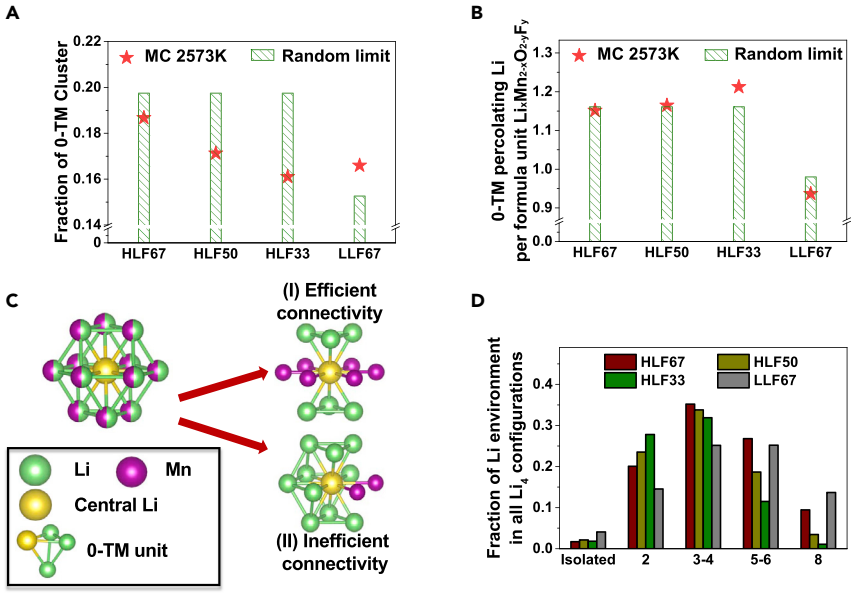

Figure 4. SRO Analysis of Li-Mn-O-F Compounds

(A) Fraction of 0-TM tetrahedral clusters in Li-Mn-O-F compounds obtained from the simulated MC structures at 2,573 K and random limit (infinite temperature).

(B) Amount of 0-TM-connected Li (percolating Li) per formula unit and comparison with random limits in Li-Mn-O-F compounds.

(C) Illustration of representative local bonding configurations around a central Li (highlighted in yellow), with green spheres and purple spheres referring to Li and Mn ions, respectively. Configuration I presents an "efficient" Li connectivity with the central Li shared by two 0-TM units; configuration II presents an "inefficient" way to create an extended percolation network, where five 0-TM units are highly localized.

(D) Distribution of different bonding environments around all the Li that are presented in 0-TM tetrahedrons: the x axis represents the number of 0-TM units sharing one Li.

clear that fluorination generally leads to a higher number of tetrahedra being occupied with Li_4. This is consistent with the previously established idea that a F^- anion in DRX materials wants to maximize the Li content around it.[20,21] The Li-rich octahedra around F^- predispose the tetrahedra with which they share three cations to be Li_4. The ability of F^- to create more Li_4 tetrahedra is clear when comparing LLF67, which has a larger fraction of them than HLF33, despite containing less Li. However, good Li transport requires connectivity of these Li_4 tetrahedra, and this is where F seems to have the largest perturbing effect. Figure 4B presents the amount of Li connected to the percolating network. Lowering the F content from HLF67 to HLF50, and HLF33, increases the amount of percolating Li despite the fact that the fraction of Li_4 tetrahedra decreases. These trends with F content indicate that F modifies the connectivity of the Li_4 tetrahedra in a very significant way. Li diffusion throughout the bulk materials only benefits from Li_4 tetrahedra that create an efficient percolating network through the material. Highly localized Li clusters, for example, where one Li is shared by five 0-TM tetrahedrons or more (as illustrated in Figure 4C), will trap a lot of Li within small domains and prevent the formation of an extended network of 0-TM tetrahedra, thus reduce the "efficiency" of 0-TM connectivity. Figure 4D shows the fraction of Li in Li_4 tetrahedra in all compounds, where the different Li environments are classified according to the number of 0-TM units around a central Li. Both "isolated" and highly shared Li ions are detrimental for transport, as they have limited contributions to the overall percolation. We can see that in HLF67 and LLF67, a larger fraction of 0-TM Li is shared by more than five 0-TM units, whereas for

HLF50 and HLF33, a larger fraction of the 0-TM Li is shared by two to four 0-TM units, which is a more "efficient" way to connect all the 0-TM tetrahedrons. The influence of different Mn valence states on the distribution of F is also investigated but is proven to be less important than the competition between Li-F and Mn-F, as discussed in Figure S9 and Note S3. The correlation between discharge capacity changes and the 0-TM percolating Li fraction in Figure 4B shows that this percolation behavior, rather than just simply the amount of Li_4 tetrahedra, is the relevant factor that controls initial capacity.

Equipped with an enhanced understanding of the charge compensation process and Li-transport property in these Li-Mn-O-F compounds, we discuss in the next section the trade-offs between initial capacity and capacity retention and rationalize some general design principles in a practical compositional space $Li_xMn_{2-x}O_{2-y}F_y$ ($1.167 \leq x \leq 1.333$, $0 \leq y \leq 0.667$).

DISCUSSION

TM Redox Capacity and Li-Site Distribution

Figure 5A summarizes the theoretical Li and Mn capacities, accessible 0-TM capacities predicted by MC simulations, and experimental capacities obtained from the first charge and discharge at 20 mA g^{-1} within the voltage window of 1.5–4.8 V for the Li-Mn-O-F compounds. Although both the TM capacity and Li-site distribution can significantly affect the cycling performance of Li-Mn-O-F compounds, their effects appear in a different manner. Comparing HLF67, HLF50, and HLF33, we observe that by increasing the amount of 0-TM percolating Li, the initial charge-discharge capacity of the compounds increases, even though the Mn-redox capacity decreases. This trend is further confirmed by the LLF67 compound, which has the lowest theoretical Li capacity and highest Mn-redox capacity but delivers the lowest initial charge-discharge capacity. These results indicate that the initial capacity does not depend on the Mn-redox capacity but is more related to the Li percolation properties. However, the Mn capacity does strongly influence the capacity decay of the materials upon extended charge-discharge cycling. As observed in Figures 2 and S5, the capacity retention improves in the order HLF33 < HLF50 < HLF67 < LLF67, consistent with the increase of Mn-redox capacity. To strengthen our hypothesis, we selected two additional compositions: DRX-Li_2MnO_3, which has more than 95% of its Li ions in the percolating network, based on our calculation, and $Li_{1.1667}Mn(II)_{0.3333}Mn(III)_{0.5}O_{1.3333}F_{0.6667}$ (denoted as L167F67), with a high theoretical Mn-redox capacity which matches its theoretical Li capacity. Both materials were synthesized using a similar mechanochemical ball-milling method described for the other samples. The voltage profiles (first cycle) and cyclability of both compounds together with those of the four previously studied compounds are presented in Figures 5B and 5C, respectively. We can see that DRX-Li_2MnO_3 exhibits the highest initial charge capacity but the worst capacity retention, whereas L167F67F displays the opposite behavior, consistent with our analysis that Li percolation controls initial capacities, while Mn-redox content controls capacity retention.

Based on these insights, we generate in Figure 5D a capacity map for Li-Mn-O-F compounds as function of the Li-excess content (x axis) and fluorine content (y axis). The color scale gives the calculated total amount of percolating Li per f.u. at each composition, and the solid lines indicate the theoretical Mn-redox capacity. Ideally, a material would have a high amount of percolating Li as well as high Mn-redox capacity, but Figure 5D shows that there is clearly a trade-off between these two. Along the x axis, Li excess is increased at the cost of Mn-redox capacity leading

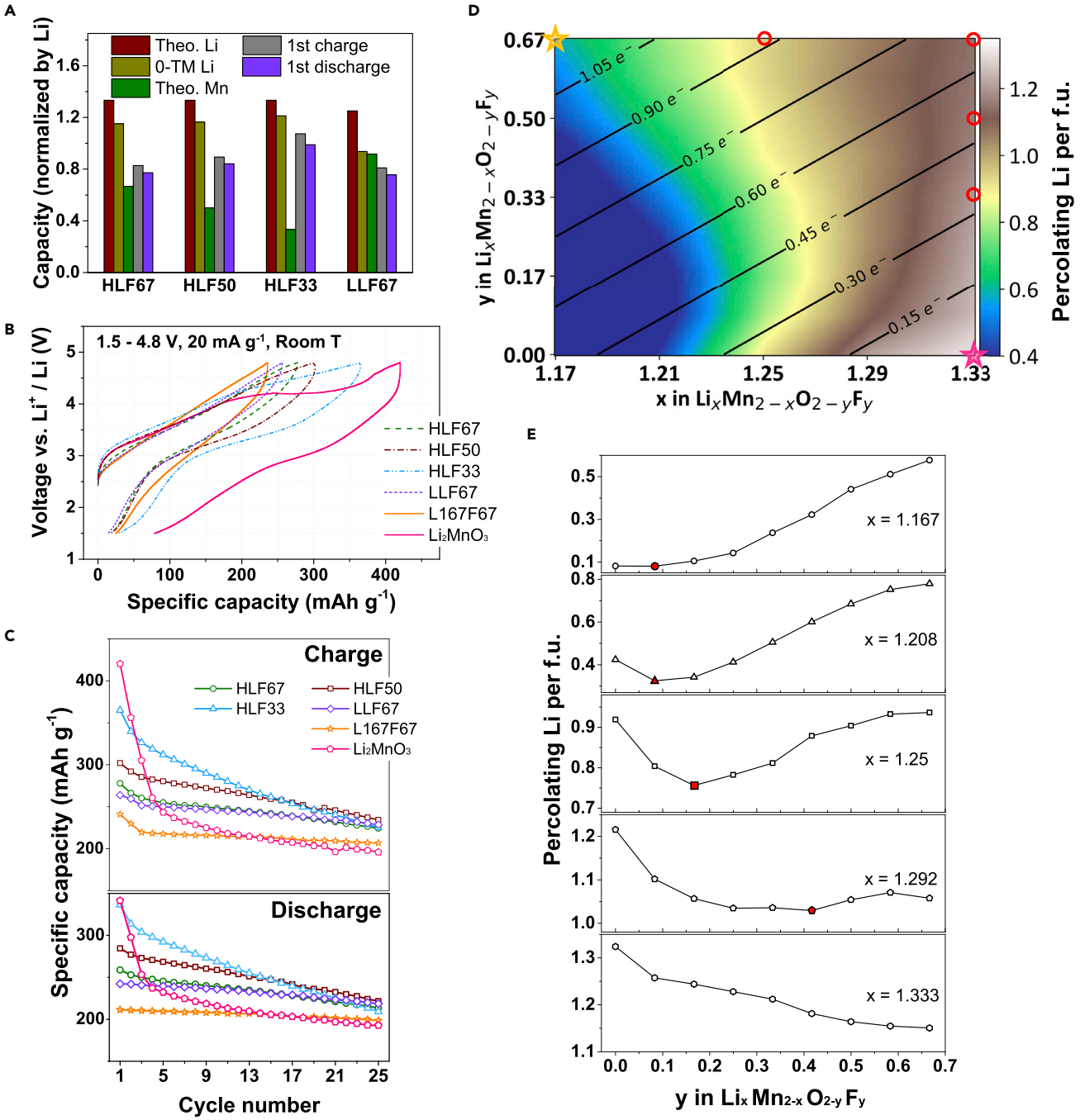

Figure 5. Design Analysis for Li-Mn-O-F Compounds

(A) Comparison of the theoretical Li/Mn-redox capacities, accessible 0-TM capacities predicted by Monte Carlo simulations, and experimental capacities obtained from the first charge-discharge at 20 mA g^{-1} at room temperature within the voltage window of 1.5–4.8 V for HLF67, HLF50, HLF33, and LLF67.

(B) Experimental first cycle voltage profiles.

(C) Cyclability for all the Li–Mn–O–F compounds at 20 mA g^{-1} at room temperature within a voltage window of 1.5–4.8 V.

(D) Design map within the Li-Mn-O-F DRX space. The color scale maps the total amount of percolating Li per f.u. through 0-TM percolation network at each composition, obtained from Monte Carlo simulations at 2,573 K. The solid lines and numbers in the map indicate the theoretical Mn-redox capacity. The red circles mark the compositions that are studied in previous sections. The pink and yellow stars mark the composition with the highest amount of 0-TM Li (DRX-Li_2MnO_3) and the highest Mn-redox capacity (L167F67 and $Li_{1.1667}Mn(II)_{0.3333}Mn(III)_{0.5}O_{1.3333}F_{0.6667}$) in the map, respectively.

(E) Li percolation analyses in $Li_xMn_{2-x}O_{2-y}F_y$ as a function of F (y values) at various Li-excess levels (x values). The critical F contents (local minimum) are highlighted in red.

to a higher fraction of percolating Li. This is expected to increase the initial discharge capacity but with rapid capacity fade. The percolation properties as a function of F content with fixed Li excess behave in a more complicated manner. In general, upon increasing F content at fixed Li excess, the fraction of percolating Li decreases initially but then increases. This trend intuitively makes sense: when the fluorination level is low, the presence of F ions attracts Li around them forming Li-rich clusters that do not percolate because their concentration—determined by the F content—is not high enough for those Li-rich clusters to connect and percolate through the sample. When the F content further increases, the Li-rich clusters around F connect together and the overall percolation improves. The Li percolation properties as a function of F content are presented at five different Li-excess levels calculated from Monte Carlo simulations: x = 1.167, 1.208, 1.25, 1.292, and 1.333 in $Li_xMn_{2-x}O_{2-y}F_y$, as shown in Figure 5E. The critical F concentration (marked in red) at which percolation starts to improve with F content increases with Li excess, and for x = 1.33, the fraction of percolating Li actually decreases with F content for the complete range shown on the map. It is possible that a critical F content can be found for y > 0.67, but we do not consider that range here due to the difficulty in synthesizing the very high-F-content materials. This map will be useful in guiding experimental design within the Li-Mn-O-F space to identify good candidates with both large 0-TM Li capacity and adequate Mn-redox capacity, e.g., those with metal-redox capacity larger than 0.6 e^- per f.u. and percolating Li amount larger than 0.7 per f.u. Considering the general presence of SRO[23] and facile oxygen redox[27,28] in DRX materials, our general findings within the Li-Mn-O-F DRX chemical space are expected to remain valid in other DRX chemical spaces.

Conclusions

In this work, we investigated Li-Mn-O-F DRX oxyfluorides that form a very promising chemical space to create high-energy, resource-light cathodes. We systematically studied four representative compounds combining electrochemical tests, spectroscopy, and modeling and demonstrated reversible capacities between 200 and 350 mAh g^{-1}. We found that the Li-site distribution plays a more important role in determining the initial capacity, whereas the metal-redox capacity is more important for determining the cyclability of the material. This intrinsic trade-off in DRX materials is related to the role of oxygen redox: increasing Li excess leads to better Li transport in DRXs but results in a larger reliance on oxygen redox to achieve high capacity and thus worse cyclability. Fluorination can compensate for this to some extent by enabling more metal-redox capacity, but its presence modifies the Li network in a significant way. A capacity map, which includes both the Li percolation properties and Mn-redox capacities, is presented to provide further guidance for experimental design in this Li-Mn-O-F chemical space.

EXPERIMENTAL PROCEDURES

Synthesis

All Li-Mn-O-F compounds were synthesized by mechanochemical ball milling. Li_2O (Alfa Aesar, ACS, 99% min), MnO (Sigma-Aldrich, 99.99%), Mn_2O_3 (Alfa Aesar, 99%), MnO_2 (Alfa Aesar, 99.9%), and LiF (Alfa Aesar, 99.99%) were used as precursors. Precursors were stoichiometrically mixed according to charge balance with a Retsch PM 200 Planetary Ball Mill at a rate of 300 rpm for 2 h. The mixed precursors were then ball-milled at 500 rpm in argon-filled stainless-steel ball-mill jars, using a Retsch PM 200 Planetary Ball Mill. The duration of ball-mill synthesis for HLF67, HLF50, HLF33, and LLF67 is 40 h and for L167F167 and Li_2MnO_3, 55 h. The total amount of precursors was 1 g. The grinding media were five 10 mm (diameter) stainless balls and ten 5 mm (diameter) balls.

Electrochemistry

All cathode films were composed of active materials, SUPER C65 (Timcal), and polytetrafluoroethylene (PTFE, DuPont, Teflon 8A) at a weight ratio of 70:20:10. To make the cathode films, 280 mg of active materials and 80 mg of SUPER C65 were mixed and shaker-milled for 1 h in an argon atmosphere with SPEX 800 M Mixer/Mill, and PTFE was later added and manually mixed with the shaker-milled mixture for 40 min. The components were then rolled into thin films inside the glovebox. Commercialized 1 M $LiPF_6$ in ethylene carbonate (EC) and dimethyl carbonate (DMC) solution (volume ratio 1:1) was used as electrolyte. Glass microfibers (Whatman) were used as separator. FMC Li-metal foil was used as anode. Coin cells were assembled inside the glovebox and tested on an Arbin battery-test instrument at room temperature. The loading density of the films was approximately 3 mg cm^{-2} based on active materials. The specific capacities were then calculated based on the weight of active materials (70%) in the cathode films. Potentiostatic intermittent titration technique (PITT) measurements were conducted on the same electrode for HLF67, HLF50, HLF33, and LLF67 to obtain quasi-equilibrium voltage profiles. All materials were charged from the open-circuit voltages to 4.8 V with a 0.01 V step interval, and the voltage was held constant for 1 h at each step.

Characterization

X-ray diffraction (XRD) patterns for the as-synthesized compounds were collected using a Rigaku MiniFlex diffractometer (Cu source) in a 2θ range of 5°–85°. Rietveld refinement was done with PANalytical X'pert HighScore Plus software. Elemental analysis was performed by Luvak Inc. with direct-current plasma-emission spectroscopy (ASTM E 1079–12) for Li and manganese and with an ion-selective electrode (ASTM D 1179–10) for fluorine. Scanning electron microscopy (SEM) images were collected using a Zeiss Gemini Ultra-55 Analytical Field Emission SEM in the Molecular Foundry at Lawrence Berkeley National Lab (LBNL). Scanning transmission electron microscopy (STEM) energy dispersive spectroscopy (EDS) measurements were performed on a JEM-2010F microscope in the Molecular Foundry at LBNL. Neutron power diffraction was measured at Nanoscale Ordered Materials Diffractometer (NOMAD) at the Spallation Neutron Source at Oak Ridge National Laboratory. The neutron-pair-distribution function (NPDF) refinement was performed using PDFGui software.[29]

Solid-State Nuclear Magnetic Resonance Spectroscopy

^{19}F and ^{7}Li NMR data on the as-synthesized HLF67, HLF50, and LLF67 powder samples were obtained at room temperature using a Bruker Avance 500 MHz (11.7 T) wide-bore NMR spectrometer, at Larmor frequencies of −470.7 MHz and −194.4 MHz, respectively. The spectra were acquired under 50 kHz magic angle spinning (MAS), using a 1.3 mm double-resonance probe, and chemical shifts were referenced against lithium fluoride powder (LiF, $\delta(^{19}F) = -204$ ppm and $\delta(^{7}Li) = -1$ ppm).

Because the resonant frequency range of the ^{19}F nuclei in the as-synthesized HLF67, HLF50, and LLF67 cathodes is larger than the excitation bandwidth of the radio frequency (RF) pulse used in the NMR experiment, nine spin-echo spectra were collected for each sample, with the irradiation frequency varied in steps of 250 ppm or 118 kHz from −1,200 ppm to 800 ppm. The individual sub-spectra were processed using a zero-order phase correction so that the on-resonance signal was in the absorption mode. The four sub-spectra were then added to give an overall sum spectrum with no further phase correction required. This "frequency stepping,"[30,31] "spin-echo mapping,"[32] or "variable offset cumulative spectrum"[33] (VOCS) methodology provides a large excitation bandwidth with uniform excitation

of the broad ^{19}F signals. Individual ^{19}F spin-echo spectra were collected using a 90° RF excitation pulse of 1.6 μs and a 180° RF pulse of 3.2 μs at 76.3 W (or 156 kHz), with a recycle delay of 50 ms. For comparison, a spin-echo spectrum was collected on LiF using similar RF pulses but a longer recycle delay of 14 s. A ^{19}F probe background spin-echo spectrum, acquired under the same conditions as the individual LMVF20 spin-echo spectra but on an empty rotor, revealed the presence of a low-intensity background signal.

^{7}Li spin-echo spectra were collected on the HLF67, HLF50, and LLF67 cathode powders using a 90° RF pulse of 0.9 μs and a 180° RF pulse of 1.8 μs at 110 W and a recycle delay of 30 ms.

Ex Situ Hard X-Ray Absorption Spectroscopy

The X-ray absorption near-edge spectroscopy (XANES) of Mn K-edge was acquired in transmission mode at beamline 20-BM-B in Advanced Photon Source. The incident beam energy was selected using a Si (111) monochromator. The energy calibration was performed by simultaneously measuring the spectra of appropriate metal foil. Harmonic rejection was accomplished using a Rh-coated mirror. All the *ex situ* samples were electrode films, composed of active materials, SUPER C65, and PTFE with weight ratio of 70:20:10, and loading density of 5 mg cm^{-2} (based on active materials). They were assembled as coin cells, charged to designated capacities, and then disassembled and washed with DMC in glovebox (except for pristine materials). Additional spectra of reference standards were also measured to facilitate the interpretation. The raw data were normalized and calibrated using Athena software.[34]

Differential Electrochemical Mass Spectrometer Measurement

The custom-built DEMS, cell geometry, and instrument operation is described in previous publications.[35–37] The electrochemical cells used with the DEMS device were prepared in glove box using modified Swagelok design and the cathode film is composed of active materials, carbon black, and PTFE with weight ratio of 70:20:10, and loading density of ~10 mg cm^{-2} (based on active materials). The electrolyte, separators, and anodes used were identical to those used for the coin cell tests in this study. The assembled cells were charged at 20 mA g^{-1} under a static head of positive argon pressure (around 1.2 bar) at room temperature after being appropriately attached to the DEMS.

Computational Methods

A combination of density functional theory (DFT) calculations together with cluster expansion Monte Carlo simulations as described in previous reports[14,20] has been applied to understand the energetics, SRO, and Li percolation in the LiF-MnO-$LiMnO_2$-Li_2MnO_3 compositional space. Using the DFT energy of 1019 structures, a cluster expansion for cation occupancy in the rocksalt structure consisting of pair interactions up to 7.1 Å, triplet interactions up to 4.0 Å, and quadruplet interactions up to 4.0 Å was fitted. The effective cluster interactions and dielectric constant were obtained from a L_1-regularized least-squares regression,[38] with the regularization parameters chosen to minimize cross-validation error.[38] By this procedure, a root-mean-squared error below 7 meV/atom has been obtained.

The DFT calculations have been performed with the Vienna *ab initio* simulation package (VASP)[39] and the projector-augmented wave (PAW) method.[40] For each of the structural optimization calculations, a reciprocal space discretization of 25 Å is applied, and the convergence criteria are set as 10^{-6} eV for electronic loops and

0.02 eV/Å for ionic loops. The PBE exchange correlation, functional with the rotationally averaged Hubbard U correction,[41] has been applied for obtaining more accurate DFT energetics, the U parameters are chosen from a previously reported calibration to oxide formation energies[42] (3.9 eV for Mn).

SRO and percolation information was obtained from canonical Monte Carlo sampling of fully lithiated structure using the Metropolis-Hastings algorithm.[43,44] To guarantee good statistics, percolation analysis and SRO for each composition and temperature are averaged over 500 structures with each consist of 6 × 6 × 8 supercells with 576 atoms.

To evaluate the voltage curve and redox mechanism, all possible Li vacancy ordering in small supercells are enumerated with energies calculated by the SCAN meta-GGA exchange correlation functional,[45] which provides a more accurate ranking of structural energetics.[46,47] With energetics evaluated by SCAN, the delithated cluster expansion is then fitted as an offset from a baseline of formal charge electrostatics. The various oxidation states of Mn and O were treated as different species and were identified according from the magnetic moment on these species in the SCAN calculations. The final root-mean-square error of this cluster expansion is less than 5 meV/atom. With this cluster expansion, the most stable Li vacancy ordering at each delithiation stage has been fully optimized using DFT for constructing the voltage curve. The pymatgen code[48] has been utilized for all the structure analysis and post-processing.

SUPPLEMENTAL INFORMATION

Supplemental Information can be found online at https://doi.org/10.1016/j.chempr.2019.10.001.

ACKNOWLEDGMENTS

This work was supported by the Umicore Specialty Oxides and Chemicals and the Assistant Secretary for Energy Efficiency and Renewable Energy of the US Department of Energy (DOE) Vehicle Technologies Office (contract DEAC02-05CH11231) under the Advanced Battery Materials Research Program. Work at the Molecular Foundry was supported by the US DOE Office of Science and Office of Basic Energy Sciences (contract DE-AC02-05CH11231). The NMR experimental work used the shared facilities of the UCSB MRSEC (National Science Foundation [NSF] DMR 1720256), a member of the Materials Research Facilities Network. This research used resources of the Advanced Photon Source, a US DOE Office of Science user facility operated by Argonne National Laboratory, and was supported by the US DOE under contract DE-AC02-06CH11357. This research used resources at the Spallation Neutron Source, a DOE Office of Science user facility operated by the Oak Ridge National Laboratory. The computational analysis was performed using computational resources sponsored by the DOE Office of Energy Efficiency and Renewable Energy and located at the National Renewable Energy Laboratory. Computational resources were provided by Extreme Science and Engineering Discovery Environment, which was supported by NSF grant ACI1053575 and the National Energy Research Scientific Computing Center, a user facility supported by the DOE Office of Science (contract DE-AC02-05CH11231). J.K.P. gratefully acknowledges support from the NSF Graduate Research Fellowship (contract DGE-1106400). The authors thank Dr. Hyunchul Kim and Dr. Nongnuch Artrith for helpful discussion, Mr. Jingyang Wang for help with XAS measurement, and Dr. Jue Liu for help with neutron diffraction measurement.

AUTHOR CONTRIBUTIONS

Z.L. planned the project with G.C.; Z.L. designed, synthesized, characterized (XRD), and electrochemically tested the proposed compounds with help from Z.C., H.J., and H.K.; B.O. performed Monte Carlo and DFT calculations and analyzed the data with help from D.A.K.; R.J.C. acquired and analyzed the NMR data; Z.L. acquired and analyzed the XAS data with the help of M.B. and J. H.; D.-H.K. acquired and analyzed TEM data; J.K.P. acquired and analyzed DEMS data with input from B.D.M.; Y.T. performed SEM. The manuscript was written by Z.L. and was revised by R.J.C., D.A.K., H.J., and G.C. with the help of the other authors. All authors contributed to discussions.

DECLARATION OF INTERESTS

The authors declare no competing interests.

Received: July 23, 2019
Revised: September 10, 2019
Accepted: September 30, 2019
Published: October 24, 2019

REFERENCES AND NOTES

1. Kang, K., Meng, Y.S., Bréger, J., Grey, C.P., and Ceder, G. (2006). Electrodes with high power and high capacity for rechargeable lithium batteries. Science *311*, 977–980.

2. Xu, B., Qian, D., Wang, Z., and Meng, Y.S. (2012). Recent progress in cathode materials research for advanced lithium ion batteries. Mater. Sci. Eng. R. Rep. *73*, 51–65.

3. Turcheniuk, K., Bondarev, D., Singhal, V., and Yushin, G. (2018). Ten years left to redesign lithium-ion batteries. Nature *559*, 467–470.

4. Olivetti, E.A., Ceder, G., Gaustad, G.G., and Fu, X. (2017). Lithium-ion battery supply chain considerations: analysis of potential bottlenecks in critical metals. Joule *1*, 229–243.

5. Lee, J., Urban, A., Li, X., Su, D., Hautier, G., and Ceder, G. (2014). Unlocking the potential of cation-disordered oxides for rechargeable lithium batteries. Science *343*, 519–522.

6. Urban, A., Lee, J., and Ceder, G. (2014). The configurational space of rocksalt-type oxides for high-capacity lithium battery electrodes. Adv. Energy Mater. *4*, 1400478.

7. Yabuuchi, N. (2018). Material design concept of lithium-excess electrode materials with Rocksalt-related structures for rechargeable non-aqueous batteries. Chem. Rec. *19*, 690–707.

8. Lee, J., Kitchaev, D.A., Kwon, D.H., Lee, C.W., Papp, J.K., Liu, Y.S., Lun, Z., Clément, R.J., Shi, T., McCloskey, B.D., et al. (2018). Reversible Mn2+/Mn4+ double redox in lithium-excess cathode materials. Nature *556*, 185–190.

9. Lee, J., Seo, D.-H., Balasubramanian, M., Twu, N., Li, X., and Ceder, G. (2015). A new class of high capacity cation-disordered oxides for rechargeable lithium batteries: Li–Ni–Ti–Mo oxides. Energy Environ. Sci. *8*, 3255–3265.

10. Freire, M., Kosova, N.V., Jordy, C., Chateigner, D., Lebedev, O.I., Maignan, A., and Pralong, V. (2016). A new active Li–Mn–O compound for high energy density Li-ion batteries. Nat. Mater. *15*, 173–177.

11. Glazier, S.L., Li, J., Zhou, J., Bond, T., and Dahn, J.R. (2015). Characterization of disordered Li (1+ x) Ti2 x Fe (1–3 x) O2 as positive electrode materials in Li-Ion batteries using percolation theory. Chem. Mater. *27*, 7751–7756.

12. Chen, R., Ren, S., Knapp, M., Wang, D., Witter, R., Fichtner, M., and Hahn, H. (2015). Disordered lithium-rich oxyfluoride as a stable host for enhanced Li+ intercalation storage. Adv. Energy Mater. *5*, 1401814.

13. Lun, Z., Ouyang, B., Kitchaev, D.A., Clément, R.J., Papp, J.K., Balasubramanian, M., Tian, Y., Lei, T., Shi, T., McCloskey, B.D., et al. (2019). Improved cycling performance of Li-excess cation-disordered cathode materials upon fluorine substitution. Adv. Energy Mater. *9*, 1802959.

14. Kitchaev, D.A., Lun, Z., Richards, W.D., Ji, H., Clément, R.J., Balasubramanian, M., Kwon, D.-H., Dai, K., Papp, J.K., Lei, T., et al. (2018). Design principles for high transition metal capacity in disordered rocksalt Li-ion cathodes. Energy Environ. Sci. *11*, 2159–2171.

15. House, R.A., Jin, L., Maitra, U., Tsuruta, K., Somerville, J.W., Förstermann, D.P., Massel, F., Duda, L., Roberts, M.R., and Bruce, P.G. (2018). Lithium manganese oxyfluoride as a new cathode material exhibiting oxygen redox. Energy Environ. Sci. *11*, 926–932.

16. Hoshino, S., Glushenkov, A.M., Ichikawa, S., Ozaki, T., Inamasu, T., and Yabuuchi, N. (2017). Reversible three-electron redox reaction of Mo3+/Mo6+ for rechargeable lithium batteries. ACS Energy Lett. *2*, 733–738.

17. Yabuuchi, N., Takeuchi, M., Nakayama, M., Shiiba, H., Ogawa, M., Nakayama, K., Ohta, T., Endo, D., Ozaki, T., Inamasu, T., et al. (2015). High-capacity electrode materials for rechargeable lithium batteries: Li3NbO4-based system with cation-disordered rocksalt structure. Proc. Natl. Acad. Sci. USA *112*, 7650–7655.

18. Lee, J., Papp, J.K., Clément, R.J., Sallis, S., Kwon, D.H., Shi, T., Yang, W., McCloskey, B.D., and Ceder, G. (2017). Mitigating oxygen loss to improve the cycling performance of high capacity cation-disordered cathode materials. Nat. Commun. *8*, 981.

19. Reed, J., Ceder, G., and Van Der Ven, A. (2001). Layered-to-spinel phase transition in Li x MnO2. Electrochem. Solid State Lett. *4*, A78–A81.

20. Richards, W.D., Dacek, S.T., Kitchaev, D.A., and Ceder, G. (2018). Fluorination of lithium-excess transition metal oxide cathode materials. Adv. Energy Mater. *8*, 1701533.

21. Clément, R.J., Kitchaev, D., Lee, J., and Ceder, G. (2018). Short-range order and unusual modes of nickel redox in a fluorine-substituted disordered rocksalt oxide lithium-ion cathode. Chem. Mater. *30*, 6945–6956.

22. Kan, W.H., Deng, B., Xu, Y., Shukla, A.K., Bo, T., Zhang, S., Liu, J., Pianetta, P., Wang, B.-T., Liu, Y., et al. (2018). Understanding the effect of local short-range ordering on lithium diffusion in Li1. 3Nb0. 3Mn0. 4O2 single-crystal cathode. Chem *4*, 2108–2123.

23. Ji, H., Urban, A., Kitchaev, D.A., Kwon, D.H., Artrith, N., Ophus, C., Huang, W., Cai, Z., Shi, T., Kim, J.C., et al. (2019). Hidden structural and chemical order controls lithium transport in cation-disordered oxides for rechargeable batteries. Nat. Commun. *10*, 592.

24. Jones, M.A., Reeves, P.J., Seymour, I.D., Cliffe, M.J., Dutton, S.E., and Grey, C.P. (2019). Short-range ordering in a battery electrode, the 'cation-disordered'rocksalt Li 1.25 Nb 0.25 Mn 0.5 O 2. Chem. Commun. *55*, 9027–9030.

25. Shannon, R.D. (1976). Revised effective ionic radii and systematic studies of interatomic

distances in halides and chalcogenides. Acta Crystallogr. A *32*, 751–767.

26. Oishi, M., Fujimoto, T., Takanashi, Y., Orikasa, Y., Kawamura, A., Ina, T., Yamashige, H., Takamatsu, D., Sato, K., and Murayama, H. (2013). Charge compensation mechanisms in Li1. 16Ni0. 15Co0. 19Mn0. 50O2 positive electrode material for Li-ion batteries analyzed by a combination of hard and soft X-ray absorption near edge structure. J. Power Sources *222*, 45–51.

27. Seo, D.H., Lee, J., Urban, A., Malik, R., Kang, S., and Ceder, G. (2016). The structural and chemical origin of the oxygen redox activity in layered and cation-disordered Li-excess cathode materials. Nat. Chem. *8*, 692–697.

28. Yabuuchi, N., Nakayama, M., Takeuchi, M., Komaba, S., Hashimoto, Y., Mukai, T., Shiiba, H., Sato, K., Kobayashi, Y., Nakao, A., et al. (2016). Origin of stabilization and destabilization in solid-state redox reaction of oxide ions for lithium-ion batteries. Nat. Commun. *7*, 13814.

29. Farrow, C.L., Juhas, P., Liu, J.W., Bryndin, D., Božin, E.S., Bloch, J., Proffen, T., and Billinge, S.J. (2007). PDFfit2 and PDFgui: computer programs for studying nanostructure in crystals. J. Phys. Condens. Matter *19*, 335219.

30. O'Dell, L.A., Rossini, A.J., and Schurko, R.W. (2009). Acquisition of ultra-wideline NMR spectra from quadrupolar nuclei by frequency stepped WURST–QCPMG. Chem. Phys. Lett. *468*, 330–335.

31. Pell, A.J., Clément, R.J., Grey, C.P., Emsley, L., and Pintacuda, G. (2013). Frequency-stepped acquisition in nuclear magnetic resonance spectroscopy under magic angle spinning. J. Chem. Phys. *138*, 114201.

32. Sananes, M.T., Tuel, A., Hutchings, G.J., and Volta, J.C. (1994). Characterization of different precursors and activated vanadium phosphate catalysts by 31P NMR spin echo mapping. J. Catal. *148*, 395–398.

33. Massiot, D., Farnan, I., Gautier, N., Trumeau, D., Trokiner, A., and Coutures, J.P. (1995). 71Ga and 69Ga nuclear magnetic resonance study of β-Ga2O3: resolution of four-and six-fold coordinated Ga sites in static conditions. Solid State Nucl. Magn. Reson. *4*, 241–248.

34. Ravel, B., and Newville, M. (2005). ATHENA, ARTEMIS, HEPHAESTUS: data analysis for X-ray absorption spectroscopy using IFEFFIT. J. Synchrotron Radiat. *12*, 537–541.

35. McCloskey, B.D., Bethune, D.S., Shelby, R.M., Girishkumar, G., and Luntz, A.C. (2011). Solvents' critical role in nonaqueous lithium–oxygen battery electrochemistry. J. Phys. Chem. Lett. *2*, 1161–1166.

36. McCloskey, B.D., Scheffler, R., Speidel, A., Bethune, D.S., Shelby, R.M., and Luntz, A.C. (2011). On the efficacy of electrocatalysis in nonaqueous Li–O2 batteries. J. Am. Chem. Soc. *133*, 18038–18041.

37. McCloskey, B.D., Speidel, A., Scheffler, R., Miller, D.C., Viswanathan, V., Hummelshøj, J.S., Nørskov, J.K., and Luntz, A.C. (2012). Twin problems of interfacial carbonate formation in nonaqueous Li–O2 batteries. J. Phys. Chem. Lett. *3*, 997–1001.

38. Nelson, L.J., Hart, G.L.W., Zhou, F., and Ozoliņš, V. (2013). Compressive sensing as a paradigm for building physics models. Phys. Rev. B *87*, 035125.

39. Kresse, G., and Furthmüller, J. (1996). Efficiency of ab-initio total energy calculations for metals and semiconductors using a plane-wave basis set. Comp. Mater. Sci. *6*, 15–50.

40. Kresse, G., and Joubert, D. (1999). From ultrasoft pseudopotentials to the projector augmented-wave method. Phys. Rev. B *59*, 1758–1775.

41. Dudarev, S.L., Botton, G.A., Savrasov, S.Y., Humphreys, C.J., and Sutton, A.P. (1998). Electron-energy-loss spectra and the structural stability of nickel oxide: an LSDA+U study. Phys. Rev. B *57*, 1505–1509.

42. Wang, L., Maxisch, T., and Ceder, G. (2006). Oxidation energies of transition metal oxides within the GGA+U framework. Phys. Rev. B *73*, 195107.

43. Metropolis, N., Rosenbluth, A.W., Rosenbluth, M.N., Teller, A.H., and Teller, E. (1953). Equation of state calculations by fast computing machines. J. Chem. Phys. *21*, 1087–1092.

44. Hastings, W.K. (1970). Monte Carlo sampling methods using Markov chains and their applications. Biometrika *57*, 97–109.

45. Sun, J., Ruzsinszky, A., and Perdew, J.P. (2015). Strongly constrained and appropriately normed semilocal density functional. Phys. Rev. Lett. *115*, 036402.

46. Kitchaev, D.A., Peng, H., Liu, Y., Sun, J., Perdew, J.P., and Ceder, G. (2016). Energetics of MnO2 polymorphs in density functional theory. Phys. Rev. B *93*, 045132.

47. Zhang, Y., Kitchaev, D.A., Yang, J., Chen, T., Dacek, S.T., Sarmiento-Pérez, R.A., Marques, M.A.L., Peng, H., Ceder, G., Perdew, J.P., et al. (2018). Efficient first-principles prediction of solid stability: towards chemical accuracy. NPJ Comp. Mater. *4*, 9.

48. Ong, S.P., Richards, W.D., Jain, A., Hautier, G., Kocher, M., Cholia, S., Gunter, D., Chevrier, V.L., Persson, K.A., and Ceder, G. (2013). Python Materials Genomics (pymatgen): a robust, open-source python library for materials analysis. Comp. Mater. Sci. *68*, 314–319.